

# Radiation Drag Effects in Black Hole Outflows from Super-critical Accretion Disks via Special Relativistic Radiation Magnetohydrodynamics Simulations

Hiroyuki R. Takahashi

*Center for Computational Astrophysics, National Astronomical Observatory of Japan, Mitaka, Tokyo 181-8588, Japan*  
takahashi@cfca.jp

Ken Ohsuga

*Division of Theoretical Astronomy, National Astronomical Observatory of Japan, Mitaka, Tokyo 181-8588, Japan*  
*School of Physical Sciences, Graduate University of Advanced Study (SOKENDAI), Shonan Village, Hayama, Kanagawa 240-0193, Japan*

(accepted for publication in PASJ)

## Abstract

By performing 2.5-dimensional special relativistic radiation magnetohydrodynamics simulations, we study the super-critical accretion disks and the outflows launched via the radiation force. We find that the outflow is accelerated by the radiation flux force, but the radiation drag force prevents the outflow velocity from increasing. The outflow velocity saturates around 30 – 40% of the light speed around the rotation axis, since then the flux force balances with the drag force. Our simulations show that the outflow velocity is kept nearly constant in the regime of  $\dot{M}_{\text{BH}} \sim 10^{2-3} L_{\text{Edd}}/c^2$ , where  $\dot{M}_{\text{BH}}$  is the mass accretion rate,  $L_{\text{Edd}}$  is the Eddington luminosity, and  $c$  is the light speed. Such a faster outflow is surrounded by a slower outflow of  $\sim 0.1c$ . This velocity is also determined by force balance between the radiation flux force and the radiation drag. The radiation drag works to collimate the slower outflow in cooperation with the Lorentz force, although the faster outflow is mainly collimated by the Lorentz force. The kinetic energy is carried by the slower outflow rather than by the faster outflow. The total kinetic luminosity of the outflow as well as the photon luminosity is  $\sim L_{\text{Edd}}$ , almost independent of the mass accretion rate.

**Key words:** accretion, accretion disks — magnetohydrodynamics (MHD) — radiation: dynamics — black hole physics

## 1. Introduction

A black hole accretion disk system is one of the most energetic phenomena in the universe. A mass accretion onto the black holes results in effective release of gravitational energy. According to the mass accretion rate, three accretion modes, i.e., standard disk model, radiatively inefficient accretion flow model, and slim disk model have been proposed by Shakura & Sunyaev (1973), Ichimaru (1977), Abramowicz et al. (1988), and Narayan & Yi (1994) (see also Kato et al. 2008, for a review). Whereas above three models are established by one-dimensional approach, multi-dimensional hydrodynamic and magnetohydrodynamic (MHD) numerical simulations of the accretion disks have been performed. In MHD simulations, the phenomenological viscosity model is not used, since the disk viscosity is magnetic origin, i.e., magnetorotational instability (Hawley & Balbus 1991). However, the radiation transfer should be solved in order to investigate the luminous accretion modes.

By 2.5-dimensional radiation magnetohydrodynamics (RMHD) simulations, Ohsuga et al. (2009) for the first time succeeded in reproducing three accretion modes by one numerical code (see also Ohsuga & Mineshige 2011). They revealed that the super-critical accretion, of which the mass accretion rate is over the critical rate ( $L_{\text{E}}/c^2$ ), shines at the super-Eddington luminosity, where  $L_{\text{E}}$  is the Eddington luminosity and  $c$  is the light speed. In this case, since the huge amount of photons is mainly released towards the rotation axis of the disks, the radiation force does not prevent the mass

accretion along the disk plane (Ohsuga & Mineshige 2007). From the surface of the super-critical accretion disks, powerful jets or outflows are launched by the strong radiation force. Takeuchi et al. (2010) showed that the jets are accelerated by the radiation force and collimated by the Lorentz force. This type of jet seems to explain mildly relativistic, powerful jet from the microquasar, SS 433. However, their simulations are not fully taken account of the relativistic effect, though the maximum velocity of the jet is several 10% of the light speed.

The highly relativistic jets, of which the velocity is close to the light speed, are thought to associate with the black hole accretion flows; e.g., microquasar GRS 1915+105 (Mirabel & Rodríguez 1994; Fender et al. 1999), active galactic nuclei (Biretta et al. 1995; Giroletti et al. 2012), and gamma-ray bursts (Abdo et al. 2009; Rykoff et al. 2009). The relativistic effects should play important roles for such highly relativistic flows. For instance, the radiation drag force decelerates the outflows in contrast with the acceleration via the radiation flux force. Thus, for a non-relativistic approach, the outflow velocity should be overestimated. The relativistic RMHD simulations are required to study the radiatively-driven high-velocity outflows. Recently, special relativistic (SR) (Takahashi et al. 2013; Takahashi & Ohsuga 2013) and general relativistic (GR) (Farris et al. 2008; Zanotti et al. 2011; Roedig et al. 2012; Sądowski et al. 2013) RMHD code has been developed, and GR-RMHD simulation of the super-critical disks are initiated (McKinney et al. 2014; Sądowski et al. 2014; Sądowski et al. 2014).

In this paper, we perform 2.5-dimensional SR-RMHD sim-

ulation of the super-critical accretion disks and launching outflows. For the outflows, we investigate the deceleration via the radiation drag as well as the acceleration via the radiation flux force. The terminal velocity is determined by the balance between above two forces. This paper is organized as follows. In Section 2, we introduce basic equations, and describe initial and boundary conditions. We show global inflow-outflow structure and detailed analysis of acceleration/deceleration of the outflow in Section 3. Lastly, Section 4 is devoted to conclusions and discussion.

## 2. Basic Equations, Initial and Boundary Conditions

We solve a full set of SR-RMHD equations. Here, the Greek suffixes,  $\mu$  and  $\nu$ , take values of 0, 1, 2, and 3, while the Latin suffixes of  $i$ ,  $j$ , and  $k$  take values of 1, 2, and 3. By taking light speed  $c$  as unity hereafter, the basic equations of ideal magnetofluids consist of mass conservation equation

$$\partial_\nu(\rho u^\nu) = 0, \quad (1)$$

energy-momentum conservation,

$$\partial_\nu \left[ \left( w_g + \frac{b^2}{4\pi} \right) u^\mu u^\nu - \frac{b^\mu b^\nu}{4\pi} + \left( p_g + \frac{b^2}{8\pi} \right) \eta^{\mu\nu} \right] = G_{\text{rad}}^\mu + f_{\text{grav}}^\mu, \quad (2)$$

and induction equation,

$$\partial_\mu(u^\mu b^\nu - u^\nu b^\mu) = 0, \quad (3)$$

where  $\rho$  is the proper mass density,  $p_g$  is the gas pressure,  $u^\mu [= \gamma(1, v^j)]$  is four velocity,  $\gamma (= 1/\sqrt{1-v_i v^i})$  is the Lorentz factor, and  $\eta^{\mu\nu}$  is the Minkowski metric (of which the signature is  $[-, +, +, +]$  in the present paper). By supposing a simple  $\Gamma$ -law polytropic equation of state, the gas enthalpy,  $w_g$ , is given by

$$w_g = \rho + \frac{\Gamma}{\Gamma-1} p_g, \quad (4)$$

with  $\Gamma$  being assumed to be  $5/3$  throughout the present study. A covariant magnetic field  $b^\mu$  is related to the magnetic field in laboratory frame,  $B^j$ , as

$$b^\mu = \left[ u_i B^i, \frac{B^j + (u_i B^i) u^j}{\gamma} \right], \quad (5)$$

and an external force is described as  $f_{\text{grav}}^\mu = -\gamma^2 w_g (u^i \partial_i \psi, \partial_i \psi)$ , where  $\psi = -GM_{\text{BH}}/(r - r_S)$  is the Pseudo-Newtonian potential (Paczynski & Wiita 1980). Here,  $M_{\text{BH}}$  is the black hole mass,  $r$  is the distance from the central black hole, and  $r_S (= 2GM_{\text{BH}})$  is the Schwarzschild radius. In the present paper, we set  $M_{\text{BH}}$  to be  $10M_\odot$ .

The radiation four force,  $G_{\text{rad}}^\mu$ , is given by

$$G_{\text{rad}}^0 = -\rho \kappa_a (4\pi \gamma B - \gamma E_{\text{rad}} + u_i F_{\text{rad}}^i) - \rho \kappa_s \left[ \gamma(\gamma^2 - 1) E_{\text{rad}} + \gamma u_j u_k P_{\text{rad}}^{jk} - (2\gamma^2 - 1) u_i F_{\text{rad}}^i \right] \quad (6)$$

and

$$G_{\text{rad}}^j = -4\pi \rho \kappa_a B u^j + \rho (\kappa_a + \kappa_s) (\gamma F_{\text{rad}}^j - u_k P_{\text{rad}}^{jk}) - \rho \kappa_s u^j (\gamma^2 E_{\text{rad}} - 2\gamma u_k F_{\text{rad}}^k + u_k u_l P_{\text{rad}}^{kl}), \quad (7)$$

where  $\kappa_a = 6.4 \times 10^{22} \rho T_g^{-3.5} \text{ cm}^2 \text{ g}^{-1}$  and  $\kappa_s = 0.4 \text{ cm}^2 \text{ g}^{-1}$  are the Rosseland mean free-free absorption coefficient and the electron scattering coefficient measured in the comoving frame,  $E_{\text{rad}}$  is the radiation energy density,  $F_{\text{rad}}^i$  is the radiation flux,  $P_{\text{rad}}^{ij}$  is the radiation stress tensor,  $B$  is the blackbody intensity, and  $T_g$  is the gas temperature.

The radiation energy density and the radiation flux are solved with using the zero-th and first order moment equations of

$$\partial_t E_{\text{rad}} + \partial_j F_{\text{rad}}^j = -G_{\text{rad}}^0, \quad (8)$$

and

$$\partial_t F_{\text{rad}}^j + \partial_i P_{\text{rad}}^{ij} = -G_{\text{rad}}^j. \quad (9)$$

The blackbody intensity  $B$  is described by gas temperature  $T_g$  by

$$B = \frac{a_{\text{rad}} T_g^4}{4\pi}, \quad (10)$$

here  $a_{\text{rad}}$  is the radiation constant, and the gas temperature is determined by the Boyle–Charles’s law:

$$p_g = \frac{\rho k_B T_g}{\mu m_p}, \quad (11)$$

where  $k_B$  is the Boltzmann constant,  $m_p$  is the proton mass, and  $\mu (= 0.5)$  is a mean molecular weight. As a closure, we adopt M-1 closure in which the Eddington tensor  $D^{jk} (\equiv P_{\text{rad}}^{jk}/E_{\text{rad}})$ , is expressed as

$$D^{jk} = \frac{1-\chi}{2} \delta^{jk} + \frac{3\chi-1}{2} n^j n^k, \quad (12)$$

where

$$\chi = \frac{3+4|\mathbf{f}|^2}{5+2\sqrt{4-3|\mathbf{f}|^2}}, \quad (13)$$

$$f^j = \frac{F_{\text{rad}}^j}{E_{\text{rad}}}, \quad (14)$$

and

$$n^j = \frac{F_{\text{rad}}^j}{|\mathbf{F}_{\text{rad}}|}. \quad (15)$$

We assume the axisymmetric ( $\partial_\phi = 0$ ) and reflecting boundary at  $\theta = 0, \pi$ . At  $\theta = 0$  and  $\pi$ ,  $\rho$ ,  $p_g$ ,  $v^r$ ,  $B^r$ ,  $E_{\text{rad}}$ , and  $F_{\text{rad}}^r$  are symmetric, while others are antisymmetric. For the inner ( $r = 2r_S$ ) and outer ( $r = 534r_S$ ) boundaries, we use free boundary conditions and allow for matter and the radiation to go out but not to come in. If the radial components of the velocity and the radiative flux are positive (negative) at the innermost (outermost) grid, they are set to be zero. For the magnetic fields, we also employ the free boundary condition for the tangential components,  $B^\theta$  and  $B^\phi$ , while the normal component,  $B^r$ , is determined to satisfy  $\nabla \cdot \mathbf{B} = 0$ .

We start simulation with a low density, non-rotating, and non-magnetized corona surrounding the black hole. The coronal density is given by

$$\rho = \rho_c \exp \left\{ -\frac{\mu m_p}{k_B T_c} [\psi(r) - \psi(r = 100r_S)] \right\}. \quad (16)$$

Here  $T_c = 10^{12}\text{K}$  is the coronal temperature and  $\rho_c = 10^{-8}\text{ g cm}^{-3}$ . The radiation temperature,  $T_{\text{rad}} \equiv (E_{\text{rad}}/a_R)^{1/4}$ , is uniform as  $T_{\text{rad}} = 10^5\text{ K}$ .

Following Igumenshchev et al. (2003), we continuously inject gas inside a torus, which is located on equatorial plane and surrounding the black hole. The curvature radius of the torus and the radius of the torus tube are  $R_{\text{torus}} = 80r_S$  and  $r_{\text{torus}} = 15r_S$ , respectively. In the torus, an increment of the gas density per unit time is  $\dot{\rho}_{\text{inj}} = \dot{M}_{\text{inj}}/(2\pi^2 r_{\text{torus}}^2 R_{\text{torus}})$ , where  $\dot{M}_{\text{inj}}$  is the mass injection rate and set to be  $10^5 L_E$ . The temperature and the angular momentum of the injected matter are set to be  $10^{10}\text{K}$  and be equal to the Keplerian angular momentum at  $r = R_{\text{Kep}} = 60r_S$ . In the torus, we also inject the poloidal magnetic field at each time step, which is given by the increment of the azimuthal component of the vector potential as

$$\Delta A^\phi = \sqrt{\frac{8\pi\Delta\rho c_{s,\text{inj}}^2}{\beta_{\text{inj}}}} \frac{r_{\text{torus}} R_{\text{torus}}}{r \sin\theta} \times \exp\left[-\frac{8(r^2 + R_{\text{torus}}^2 + 2rR_{\text{torus}}\sin\theta)}{r_{\text{torus}}^2}\right], \quad (17)$$

where  $\Delta\rho = \dot{\rho}_{\text{inj}}\Delta t$  and  $c_{s,\text{inj}}$  are the increase of the mass density inside the torus within the time step,  $\Delta t$ , and the sound velocity of the injected gas, respectively. We set  $\beta_{\text{inj}} = 100$ . We compute the plasma- $\beta$  inside the torus at each time step and suspend injection of the magnetic field when plasma- $\beta$  is smaller than 30 for numerical stability (Igumenshchev 2008).

We have to note that our simulation has been performed in 2-dimension by assuming axisymmetry, so that the anti-dynamo effect works and the magnetic field cannot be maintained (Cowling 1933). So as to avoid this problem, we inject the gas which has the poloidal magnetic field, realizing a steady accretion in the present work (see, section 3.1). Our procedure would not be unnatural, since the magnetized matter is thought to be transported from outer region to the disks in reality. Also, the phenomenological dynamo model is employed to amplify the magnetic fields in some of 2-dimensional simulations (Bucciantini & Del Zanna 2013; Bugli et al. 2014; Sadowski et al. 2014). The 3-dimensional simulations, in which the anti-dynamo does not work, are performed by McKinney et al. (2014). The impact of our boundary condition on the resulting accretion flow structure should be verified by comparing results between these different models.

### 3. Results

#### 3.1. Overview

After simulation starts, a gas is injected in the torus. Since the injected gas is not in dynamically equilibrium and since a gas pressure is larger in the torus than in the corona, the injected gas expands by the gas pressure gradient force at once. This gas falls back towards the equatorial plane and accumulates around  $r = R_{\text{Kep}}$ . Such an expansion behavior is remarkable only at the elapse time of  $t \lesssim 1\text{ s}$ . After a few second, a MHD turbulence develops and gas starts to accrete onto the black hole. The mass accretion rate onto the black hole rapidly increases at  $t = 2.4\text{ s}$ . After that, the gas is continuously swallowed by the black hole at the super-critical rate,  $\gg L_E$ . Then, the radiation energy is enhanced in the accretion disks since a

part of the gas internal energy is converted through the free-free emission. The strong radiation force drives the outflows from the disks. At that time, since the torus is embedded in the dense matter, the expansion behavior does not occur. Hence, the incipient expansion does not affect the accretion motion and launching outflows.

In the left panel of Figure 1, we show the distribution of the radiation energy density (color) and the radiation flux normalized by the radiation energy density is denoted by arrows in  $R$ - $z$  plane. Here  $R(= r \sin\theta)$  and  $z(= r \cos\theta)$  are horizontal and vertical distances. A right panel indicates the density distribution (color) overlaid with the velocity vectors. Solid and dashed curves in the right panel show  $\tau_{\text{tot}} = 1$  and  $\tau_{\text{eff}} = 1$ , respectively. Here  $\tau_{\text{tot}}$  and  $\tau_{\text{eff}}$  are the total and effective optical depths integrated from  $z = \pm 300r_S$  to  $z = 0$  in  $\mp z$ -direction. We find in the right panel that the geometrically thick disk forms (red). This disk is supported by the strong radiation pressure. Indeed, it is found that the radiation energy density is enhanced in the disk. Since the disk is very optically thick for the electron scattering, most of the radiation energy is trapped inside the accretion disks.

In contrast of  $|F_{\text{rad}}| \ll E_{\text{rad}}$  in the disk, the radiation energy is effectively transported above the disk ( $z/R \gtrsim 2$ ) due to small density (small optical depth). Especially, we find  $|F_{\text{rad}}| \sim E_{\text{rad}}$  around the rotation axis, meaning that the photons freely move in vertical direction. Then, the radiation flux force effectively accelerates the gas, leading to the outflows. Such an outflowing motion is clearly shown in the right panel (see velocity vectors above the disk).

We plot in Figure 2 a time evolution of the mass accretion rate onto the black hole (thin black),

$$\dot{M}_{\text{BH}} \equiv -2\pi(2r_S)^2 \int_{-\pi}^{\pi} \gamma\rho v^r \sin\theta d\theta, \quad (18)$$

and the mass outflow rate (thick black),

$$\dot{M}_{\text{out}} \equiv 2\pi \int_0^{150r_S} \gamma\rho v^z H(v^r - v_{\text{esc}}) R dR \Big|_{z=300r_S} - 2\pi \int_0^{150r_S} \gamma\rho v^z H(v^r - v_{\text{esc}}) R dR \Big|_{z=-300r_S}. \quad (19)$$

$H$  is the Heaviside function,

$$H(x) = \begin{cases} 0 & (x < 0) \\ 1 & (x > 0) \end{cases} \quad (20)$$

and  $v_{\text{esc}} = \sqrt{r_S/r}$  is the escape velocity. Here we ignored relativistic effects since the outflow velocity is only mildly relativistic (see, Section 3.2) and the rest mass is the dominant energy density. The photon luminosity,  $L_{\text{ph}}$  (thick red), the kinetic power,  $L_{\text{kin}}$  (thick blue), the photon luminosity swallowed by the black hole,  $L_{\text{ph,BH}}$  (thin red), and the kinetic power swallowed by the black hole,  $L_{\text{kin,BH}}$  (thin blue) are also represented in this figure. These values are evaluated as

$$L_{\text{ph}} \equiv 2\pi \int_0^{150r_S} F_{\text{rad}}^z R dR \Big|_{z=300r_S} - 2\pi \int_0^{150r_S} F_{\text{rad}}^z R dR \Big|_{z=-300r_S}, \quad (21)$$

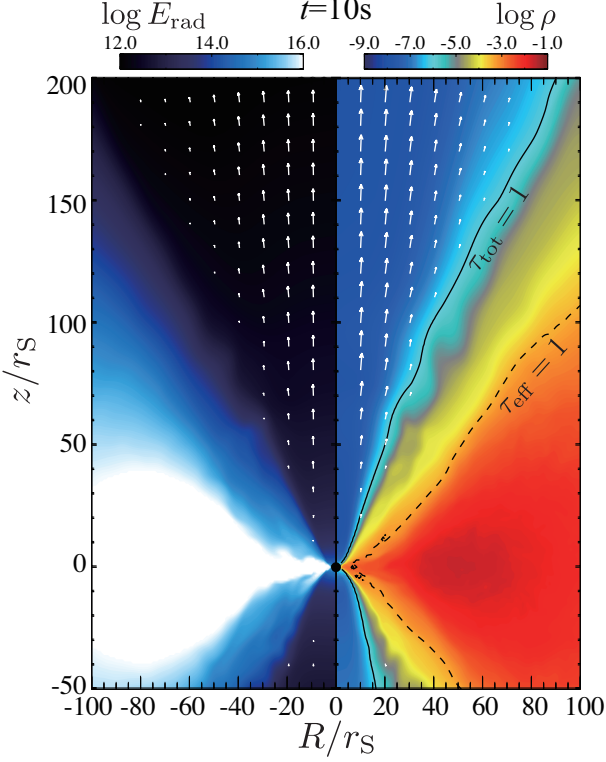


**Fig. 1.** Global structure of radiation dominated accretion disks and launching outflows at  $t = 10$  s. Color shows  $E_{\text{rad}}$  and  $\rho$  and arrows indicate  $\mathbf{F}_{\text{rad}}/E_{\text{rad}}$  and  $\mathbf{v}$  for left and right panels, respectively. Solid and dashed curves in the right panel show  $\tau_{\text{tot}} = 1$  and  $\tau_{\text{eff}} = 1$ , respectively.

$$L_{\text{kin}} \equiv 2\pi \int_0^{150r_S} \gamma(\gamma w_g - \rho) v^z H(v^r - v_{\text{esc}}) R dR \Big|_{z=300r_S} - 2\pi \int_0^{150r_S} \gamma(\gamma w_g - \rho) v^z H(v^r - v_{\text{esc}}) R dR \Big|_{z=-300r_S} \quad (22)$$

$$L_{\text{ph,BH}} \equiv -2\pi(2r_S)^2 \int_{-\pi}^{\pi} F_{\text{rad}}^r \sin \theta d\theta, \quad (23)$$

and

$$L_{\text{kin,BH}} \equiv -2\pi(2r_S)^2 \int_{-\pi}^{\pi} \gamma(\gamma w_g - \rho) v^r \sin \theta d\theta. \quad (24)$$

After  $t \simeq 3$  sec., we find that the mass accretion rate onto the black hole is about  $\dot{M}_{\text{BH}} \simeq 1000L_E$  and slowly increases with time. Due to the release of the gravitational energy via the mass accretion, the radiation energy is enhanced, driving the outflow from the accretion disk. The outflow carries a large amount of gas at the rate of  $\sim$  a few 10% of the mass accretion rate, which exceeds the critical rate ( $L_E$ ). The kinetic power and the photon luminosity are almost comparable to the critical rate, i.e.,  $L_{\text{kin}} \sim L_{\text{ph}} \sim L_E$ . In addition, we find  $L_{\text{kin}}$  and  $L_{\text{ph}}$  are much smaller than  $L_{\text{kin,BH}}$  and  $L_{\text{ph,BH}}$ , respectively. This means that most of kinetic and radiation energies are swallowed by the black hole. Since the huge amount of photons is swallowed by the black hole with accreting gas (photon trapping), the photon luminosity is not sensitive to the mass accretion rate (Begelman 1978; Ohsuga et al. 2002, 2003). This is clearly shown in Figure 3, where  $L_{\text{ph}}$  (red open circle) as

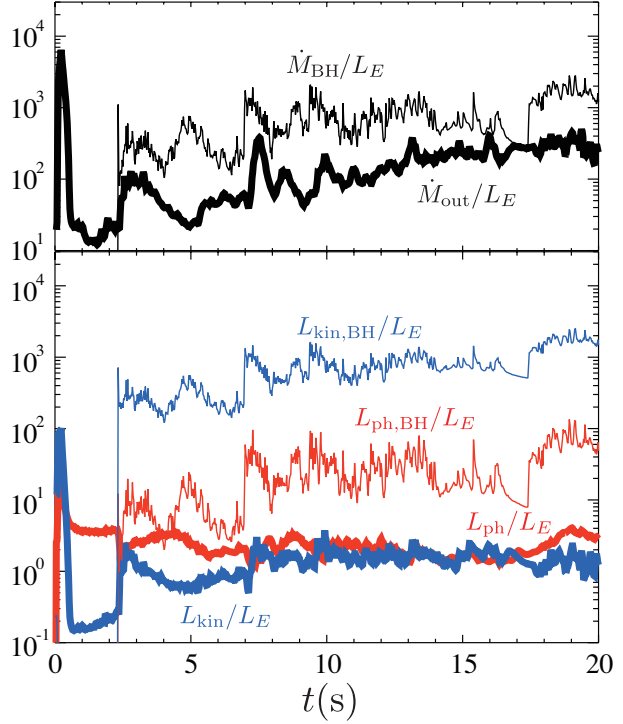


**Fig. 2.** Time evolution of the mass accretion rate onto the black hole ( $\dot{M}_{\text{BH}}$ , thick black), the mass outflow rate ( $\dot{M}_{\text{out}}$ , thin black), the photon luminosity ( $L_{\text{ph}}$ , thick red), and the kinetic power ( $L_{\text{kin}}$ , thick blue). Red and blue thin curves denote the photon luminosity and kinetic power swallowed by the black hole ( $L_{\text{ph,BH}}$  and  $L_{\text{kin,BH}}$ ), respectively.

well as  $L_{\text{ph,BH}}$  (red filled circle) is plotted as a function of the accretion rate,  $\dot{M}_{\text{BH}}$ . In contrast with  $L_{\text{ph}}$ , we find  $L_{\text{ph,BH}}$  increases with an increase of  $\dot{M}_{\text{BH}}$ . Such an effective photon trapping is a characteristic feature in super-critical accretion disks (Ohsuga et al. 2005; Ohsuga & Mineshige 2007, 2011).

We note that most of calculations in the previous study start from an initial torus, which is in hydrostatic equilibrium. In this method, the total mass within the computational domain decreases with time. In our simulations, the gas is injected at constant rate. The total mass in the simulation box and the mass accretion rate onto the black hole increases with time. However, the disk is actually in steady state which is understood in Figure 4. In this figure, we plot the mass inflow ( $\dot{M}_i$  dashed) and outflow ( $\dot{M}_o$ , dotted) rates as a function of  $r$ ,

$$\dot{M}_i(r) = -2\pi \int \gamma \rho v^r H(-v^r) r^2 \sin \theta d\theta, \quad (25)$$

and

$$\dot{M}_o(r) = 2\pi \int \gamma \rho v^r H(v^r) r^2 \sin \theta d\theta. \quad (26)$$

Here note that  $\dot{M}_i$  is the same with  $\dot{M}_{\text{BH}}$  when we take  $r = 2r_S$ . A total mass flow rate ( $\dot{M}_i - \dot{M}_o$ ) is also plotted by solid lines. We can see that the inflow rate is larger than the outflow rate, and the total mass flow rate is almost constant in the region of  $r = [2 - 30]r_S$ . This indicates that the inflow equilibrium is attained, while the mass flow rate slowly increases with time. Thus, the results obtained by our simulation are not transient



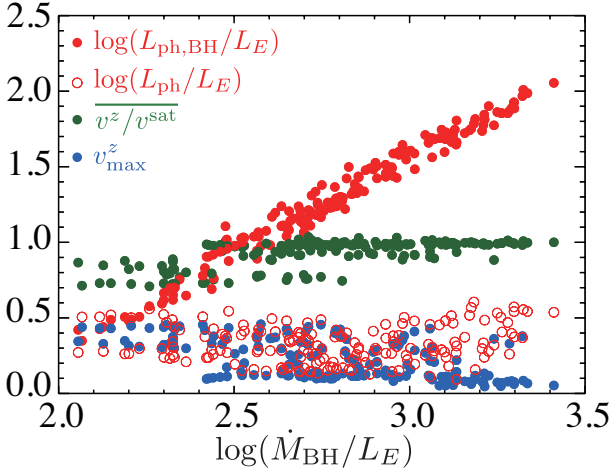


**Fig. 3.** The photon luminosity ( $L_{\text{ph}}$ , open red circle), the photon luminosity swallowed by the black hole ( $L_{\text{ph,BH}}$ , filled red circle), and the maximum outflow velocity ( $v_{\text{max}}^z$ , blue circle) as a function of  $\dot{M}_{\text{BH}}$ . Here,  $v_{\text{max}}^z$  is calculated at the surface of  $z = \pm 300r_{\text{S}}$  and  $R = [0, 150r_{\text{S}}]$ . We also plot  $v^z/v^{\text{sat}}$  (green circle), where bar denotes the averaged value at the surface of  $z = \pm 300r_{\text{S}}$  and  $R = [0, 150r_{\text{S}}]$ .

behavior but the quasi-steady structure for various mass accretion rate,  $\dot{M}_{\text{BH}}$ .

Also, Sadowski et al. (2014) showed that the mechanical energy weakly increases with  $\dot{M}_{\text{BH}}$ , while it is almost independent of it in our results. Such a discrepancy might be due to the general relativistic effects and/or  $\dot{M}_{\text{BH}}$ . In Sadowski et al. (2014), the general relativistic effects are taken into consideration and the mass accretion rate is around  $\lesssim 100\dot{M}_{\text{E}}$ . The present simulations are special relativistic version, and the mass accretion exceeds  $100\dot{M}_{\text{E}}$ . Detailed study of such a difference is left as an important future work.

### 3.2. Outflow Properties

Next, we focus on the outflow structure. We hereafter show time averaged values over  $t = 10 - 11\text{s}$ . Figure 5 shows vertical profiles of the outflow velocity,  $v^z$  for  $R = 10r_{\text{S}}$  (black solid),  $30r_{\text{S}}$  (black dashed), and  $60r_{\text{S}}$  (black dotted). We can see that a gas is accelerated at the small altitudes, and its velocity finally saturates at the outer region due to the radiation drag (we will discuss in next subsection). In particular, the outflow velocity for  $R = 10r_{\text{S}}$  is proportional to the altitude at  $\lesssim 80r_{\text{S}}$ , and is kept constant in the region of  $z \gtrsim 80r_{\text{S}}$ . For  $R = 30r_{\text{S}}$  and  $60r_{\text{S}}$ , the gas is accelerated up to  $z \sim 240r_{\text{S}}$  and  $\sim 280r_{\text{S}}$ . The terminal outflow velocity is larger near the rotation axis, where the gas is blown away at the speed of  $\sim 0.3$ . The velocity for  $R = 60r_{\text{S}}$  is slightly over 0.2 at a maximum.

Such  $R$ -dependence of the outflow velocity at  $z = 300r_{\text{S}}$  is clearly shown in Figure 6 (black solid). As noted before, the faster outflow ( $v^z \gtrsim 0.3$ ) is concentrated near the rotation axis ( $R < 30r_{\text{S}}$ ), while slower outflow extends up to  $R \sim 100r_{\text{S}}$ . Its speed is typically  $\sim 0.1 - 0.2$ , which exceeds the escape velocity (dashed line). This structure is similar to spine-sheath structure (Sol et al. 1989; Meier 2003), in which the faster outflow/jet is surrounded by the slower outflow.

In this figure, we also plot  $R$ -dependent kinematic power ( $\Delta L_{\text{kin}}$ , blue) and photon luminosity ( $\Delta L_{\text{ph}}$ , red). They are

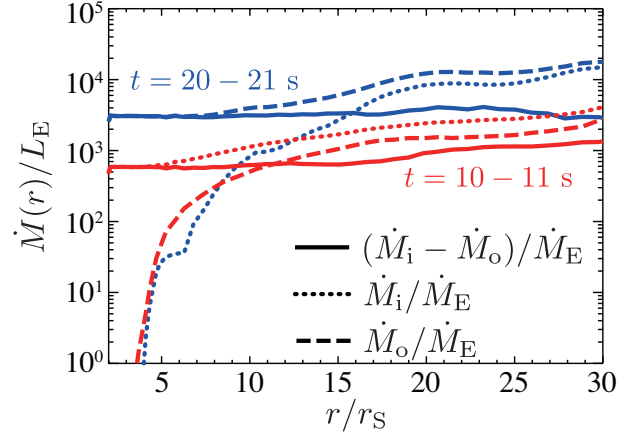


**Fig. 4.** Radial profiles of accretion rate (dashed), outflow rate (dotted) passing through the spherical surface with polar radius  $r$  averaged between  $t = 10 - 11\text{ s}$  (red) and  $t = 20 - 21\text{ s}$  (blue). The accretion rate is plotted by changing its sign. Solid curves denote for the total mass flow rate.

assessed as

$$\begin{aligned} \Delta L_{\text{kin}} \equiv & 2\pi \int_{R-\Delta R/2}^{R+\Delta R/2} \gamma(\gamma w_{\text{g}} - \rho) v^z H(v^r - v_{\text{esc}}) R dR \Big|_{z=300r_{\text{S}}} \\ & - 2\pi \int_{R-\Delta R/2}^{R+\Delta R/2} \gamma(\gamma w_{\text{g}} - \rho) v^z H(v^r - v_{\text{esc}}) R dR \Big|_{z=-300r_{\text{S}}} \end{aligned} \quad (27)$$

and

$$\begin{aligned} \Delta L_{\text{ph}} \equiv & 2\pi \int_{R-\Delta R/2}^{R+\Delta R/2} F_{\text{rad}}^z R dR \Big|_{z=300r_{\text{S}}} \\ & - 2\pi \int_{R-\Delta R/2}^{R+\Delta R/2} F_{\text{rad}}^z R dR \Big|_{z=-300r_{\text{S}}}, \end{aligned} \quad (28)$$

where  $\Delta R \equiv 2r_{\text{S}}$ . We find that the kinetic energy is mainly carried by the slower outflow. The relation of  $\Delta L_{\text{kin}} \propto R$  implies that the kinetic energy flux (the kinetic energy transported per unit surface and per unit time) is almost constant within  $R \sim 40r_{\text{S}}$ . This figure also shows that such a kinetic energy flux is larger near the rotation axis ( $R \lesssim 40r_{\text{S}}$ ) than in the region of  $R \gtrsim 40r_{\text{S}}$ . The profile of  $\Delta L_{\text{ph}}$  is similar with that of  $\Delta L_{\text{kin}}$ . Thus, the vertical radiation flux is mildly collimated within  $R \sim 40r_{\text{S}}$ . However, due to a larger opening angle, the kinetic power of the slow outflow is dominant over that of the fast outflow, and the radiation energy is mainly released from the region of  $R \sim 40 - 100r_{\text{S}}$ .

### 3.3. Radiation Drag Force

In this subsection, we show effects of the radiation drag in the outflow. Since the flow is quasi-steady, here, we introduce the steady state equation of motion,

$$\gamma^2 w_{\text{g}} (\mathbf{v} \cdot \nabla) v^j = f_{\text{gas}}^j + f_{\text{mag}}^j + f_{\text{grav}}^j + f_{\text{rad}}^j, \quad (29)$$

where

$$f_{\text{gas}}^j = -\partial_j p_{\text{g}}, \quad (30)$$

$$f_{\text{mag}}^j = \frac{1}{4\pi} [(\mathbf{v} \times \mathbf{B})^j \partial_i (\mathbf{v} \times \mathbf{B})^i] + \frac{1}{4\pi} [(\nabla \times \mathbf{B}) \times \mathbf{B}]^j,$$

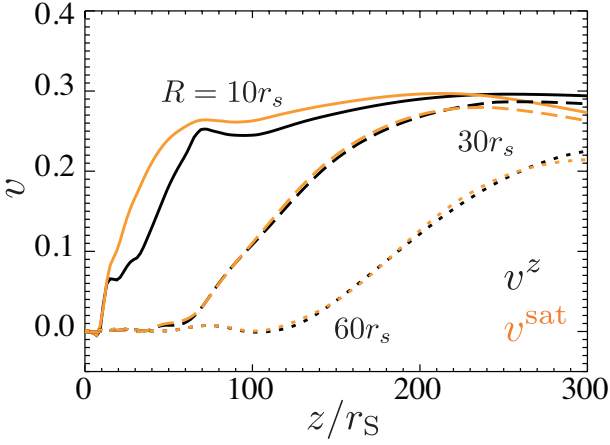


**Fig. 5.** Vertical profiles of the vertical component of the velocity ( $v^z$ , black) and the saturation velocity ( $v^{\text{sat}}$ , orange) for  $R = 10$  (solid),  $30$  (dashed),  $60r_s$  (dotted), respectively.

$$f_{\text{rad}}^j = f_{\text{rad-flux}}^j + f_{\text{rad-drag}}^j + f_{\text{rad-corr}}^j, \quad (32)$$

are the gas pressure gradient, Lorentz, and radiation forces. The radiation force consists of following three components; the radiation flux force,

$$f_{\text{rad-flux}}^j = \gamma\rho(\kappa_a + \kappa_s)F_{\text{rad}}^j, \quad (33)$$

the radiation drag,

$$f_{\text{rad-drag}}^j = -\gamma\rho(\kappa_a + \kappa_s)\left(E_{\text{rad}}v^j + v_k P_{\text{rad}}^{jk}\right), \quad (34)$$

and the relativistic correction,

$$f_{\text{rad-corr}}^j = \gamma\rho(\kappa_a + \kappa_s)(v_i F_{\text{rad}}^i)v^j. \quad (35)$$

The radiation drag, which is of the order of  $v$ , works to slow down the relativistic flow. The relativistic correction is  $\mathcal{O}(v^2)$  so that it plays an important role only for highly relativistic flow.

In a top panel of Figure 7, a vertical component of the radiation force (orange) and gravitational force (black) are plotted along the vertical lines of  $R = 10r_s$  (solid) and  $30r_s$  (dashed). We can see that the radiation force tends to be weaker than the gravity at small altitude (within the disk), but exceeds the gravity above the disk. The turn-around altitude is around  $20r_s$  for  $R = 10r_s$  and  $110r_s$  for  $R = 30r_s$ . Although the gas pressure-gradient force and the Lorentz force are not plotted in this panel, they are much smaller than the gravity. Therefore, we conclude that the outflows are accelerated by the radiation force. The gas is mainly accelerated just above the turn-around altitude since  $f_{\text{rad}}^z + f_{\text{grav}}^z$  peaks there, and the radiative acceleration becomes ineffective at large altitude. Note that the deviation between the radiation force and the gravity is significant near the rotation axis. This is the reason why the faster outflow/jet forms around the axis (see Figures 1 and 5).

Why the radiative acceleration decreases at large altitude? This is due to the radiation drag. A bottom panel of Figure 7 shows the vertical profile of  $f_{\text{rad}}^z$  (orange),  $f_{\text{rad-flux}}^z$  (red),  $-f_{\text{rad-drag}}^z$  (blue) and  $f_{\text{rad-corr}}^z$  (green) at  $R = 10r_s$ . It is found that the  $f_{\text{rad-flux}}^z$  is much larger than the gravity at large altitude. This implies that the radiation flux force continues to accelerate the gas. However, the radiation drag, which is the

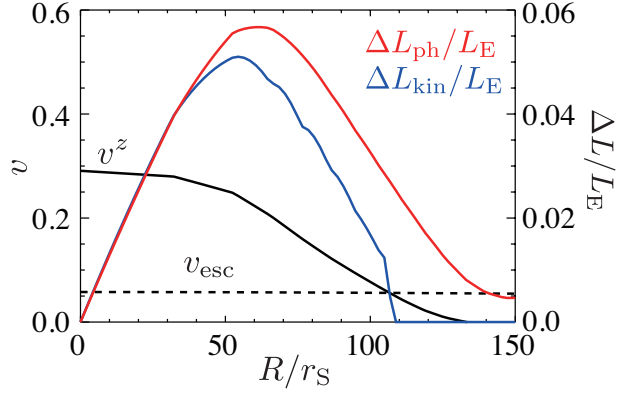


**Fig. 6.** Radial profiles of the vertical component of the velocity ( $v^z$ , black),  $\Delta L_{\text{kin}}$  (blue), and  $\Delta L_{\text{ph}}$  (red) at  $|z| = 300r_s$ . A dashed curve denotes for the escape velocity.

downward force, is comparable to the radiation flux force at  $z \gtrsim 80r_s$ . Thus, the radiative acceleration becomes inefficient at the large altitude. In contrast, the radiation flux force is much larger than the radiation drag force,  $f_{\text{rad-flux}}^z \gg -f_{\text{rad-drag}}^z$ , just above the turn-around altitude ( $z \sim 20r_s$ ), leading to the effective acceleration. Here we note that the outflow velocity is mildly relativistic so that  $f_{\text{rad-corr}}^z$  is negligible.

The force balance of  $f_{\text{rad-flux}}^z \sim -f_{\text{rad-drag}}^z$  is nearly equivalent to  $F_{\text{rad}}^{\prime z} \sim 0$ , where  $F_{\text{rad}}^{\prime z}$  is the radiation flux measured in the comoving frame. This is because that  $F_{\text{rad}}^{\prime z}$  is related to the radiation fields in the laboratory frame as  $F_{\text{rad}}^{\prime z} \sim F^z - E_{\text{rad}}v^z - v_i P_{\text{rad}}^{zi}$ , and it is rewritten as  $(f_{\text{rad-flux}}^z - f_{\text{rad-drag}}^z)/[\rho(\kappa_a + \kappa_s)]$ . From this fact, we can obtain the saturation velocity from  $F_{\text{rad}}^{\prime z} = 0$  as

$$v^{\text{sat}} = \frac{F_{\text{rad}}^z}{E_{\text{rad}} + P_{\text{rad}}^{zz}}. \quad (36)$$

Here we assume  $|v_z P_{\text{rad}}^{zz}| \gg |v_r P_{\text{rad}}^{rz}|, |v_\phi P_{\text{rad}}^{\phi z}|$ . In Figure 5, we plot the saturation velocity by orange lines. This figure clearly shows  $v^z < v^{\text{sat}}$  at  $z \lesssim 220$  for  $R = 10r_s$ . In this region, the vertical component of the radiation flux in the comoving frame is positive and the gas is pushed in the vertical direction. We find  $v^z \sim v^{\text{sat}}$  above that region, implying that the radiation flux is almost zero in the comoving frame. The radiation force thus cannot accelerate a gas further. In this figure, we can also see that  $v^z$  is slightly less than  $v^{\text{sat}}$  at  $z \lesssim 200r_s$  for  $30r_s$ , leading to the weak acceleration of the gas.

This radiation drag plays an important role when  $\dot{M}_{\text{BH}} \gg L_E$ . In figure 3, we show a maximum outflow velocity,  $v_{\text{max}}^z$  (blue), which is computed at a surface of  $|z| = 300r_s$  and  $R = [0, 150r_s]$ . We also plot a ratio of saturation velocity and outflow velocity averaged over the same surface for maximum outflow velocity,  $\overline{v^z/v^{\text{sat}}}$  (green). This figure shows that the maximum velocity is about  $0.1 - 0.4$ , and it is not so sensitive to the mass accretion rate. We also find that  $\overline{v^z/v^{\text{sat}}}$  is very close to unity independently of the mass accretion rate, although we find  $\overline{v^z/v^{\text{sat}}} \lesssim 1$  at the range of  $\dot{M}_{\text{BH}} \lesssim 10^{2.5} L_E$ . It means that the outflow velocity is determined by the force balance between the radiation drag and the radiation flux force. The maximum velocity of the radiatively driven outflow/jet from the super-critical accretion disks cannot largely exceed

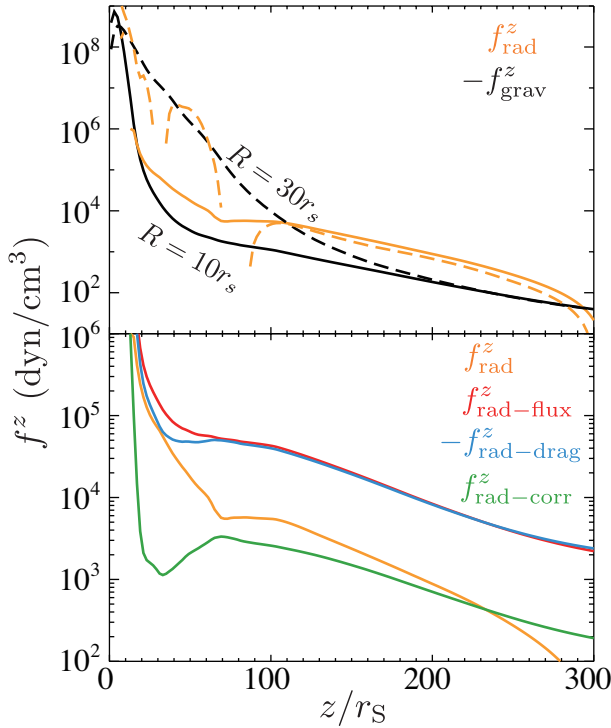


**Fig. 7.** Vertical component of the force densities as a function of the altitude,  $z$ . Top panel: the gravity ( $-f_{\text{grav}}^z$ , black) and the radiation force ( $f_{\text{rad}}^z$ , orange) for  $R = 10r_s$  (solid) and  $30r_s$  (dashed). Bottom panel: the radiation flux force ( $f_{\text{rad-flux}}^z$ , red), the radiation drag force ( $-f_{\text{rad-drag}}^z$ , blue), and the relativistic correction ( $f_{\text{rad-corr}}^z$ , green) at  $R = 10r_s$ . The orange curve is the same as that of the top panel ( $f_{\text{rad}}^z$ ).

a few 10% of the light velocity.

The saturation velocity given in equation (36) is obtained by assuming that  $|v^z P_r^{zz}| \gg |v^R P_r^{Rz}|, |v^\phi P_r^{\phi z}|$ . This assumption comes from the fact that the diagonal terms of the radiation pressure dominates over the off-diagonal terms. This result does not change even if we apply the Eddington approximation instead of M-1 closure. We calculated the off-diagonal terms using the Eddington approximation, and confirmed that the diagonal terms are larger than off-diagonal terms. The difference of the radiation dragging force is less than 1%, implying that the saturation velocity does not change so much. It is, however, noted that the radiation pressure tensor in the Eddington approximation is computed based on  $E_{\text{rad}}, F_{\text{rad}}^i$ , and  $u^i$  obtained from the present simulation. If the numerical simulations with the Eddington approximation is performed, we may obtain the different results since the Eddington approximation gives the different radiation flux from the M-1 method (Takahashi & Ohsuga 2013; see also Section 4).

Here it seems that the terminal velocity approaches to 0.5 in the free streaming limit (e.g.,  $F_{\text{rad}}^z = E_{\text{rad}}, P_{\text{rad}}^{zz} = E_{\text{rad}}$ ) according to equation (36). This is because we ignored the relativistic correction,  $f_{\text{rad-corr}}^j$ . If we take into account this term correctly, and if we assume  $F_{\text{rad}}^z = E_{\text{rad}}$  (and  $P_{\text{rad}}^{zz} = E_{\text{rad}}$ ), the terminal velocity approaches to the light speed. Although we have  $F_{\text{rad}}^z < E_{\text{rad}}$  and  $v \ll 1$  in the present simulations since the radiation comes from the funnel-shaped photosphere of the disk,  $F_{\text{rad}}^z$  does approach to  $E_{\text{rad}}$  at very large altitude.

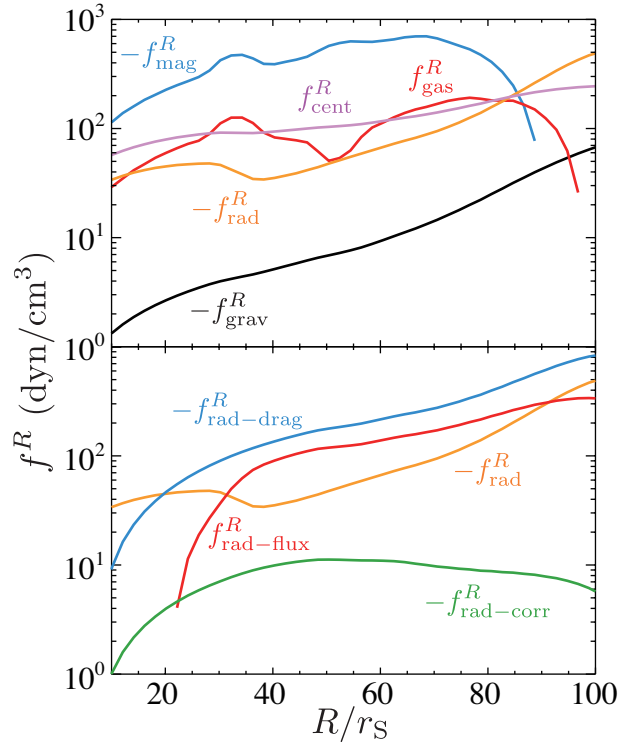


**Fig. 8.** Horizontal component of the force densities at  $z = 300r_s$  as a function of  $R$ . Top panel: the gravity ( $-f_{\text{grav}}^R$ , black), the radiation force ( $-f_{\text{rad}}^R$ , orange), the gas pressure gradient force ( $f_{\text{gas}}^R$ , red), the centrifugal force ( $f_{\text{cent}}^R$ , magenta), and the Lorentz force ( $-f_{\text{mag}}^R$ , blue). Bottom panel: The radiation flux force ( $f_{\text{rad-flux}}^R$ , red), the radiation drag force ( $-f_{\text{rad-drag}}^R$ , blue), and the relativistic correction ( $-f_{\text{rad-corr}}^R$ , green). The orange curve is the same as that of the top panel ( $-f_{\text{rad}}^R$ ).

But then, the radiation is attenuated and the gas would not be effectively accelerated.

In cooperation with the Lorentz force, the radiation drag also plays an important role for the collimation of the outflow. A top panel of figure 8 shows the horizontal component of the force densities at  $z = 300r_s$ . Black, orange, red, magenta, and blue curves denote for the force densities due to the gravitational force, the radiation force, the gas pressure gradient force, the centrifugal force, and the Lorentz force. At the regime of  $R \lesssim 100r_s$ , the gravitational and the Lorentz forces are negative (i.e.,  $-R$  direction), while the gas pressure gradient and centrifugal forces are positive. The sum of  $f_{\text{gas}}^R$  and  $f_{\text{cent}}^R$  approximately balances with the Lorentz force. This implies that the gas pressure gradient and centrifugal forces work to expand the outflow in  $R$ -direction, in contrast that the Lorentz force collimates the outflow. Such a result is similar with the result of non-relativistic RMHD simulations (Takeuchi et al. 2010), in which the centrifugal force balances with the Lorentz force. At the far region,  $R \gtrsim 80r_s$ , the radiation force has a negative value and is dominant over the other forces.

Negative value of the radiation force is responsible for the radiation drag. It is clearly seen in a bottom panel of Figure 8. In this panel, we plot  $-f_{\text{rad}}^R$  (orange),  $f_{\text{rad-flux}}^R$  (red),  $-f_{\text{rad-drag}}^R$  (blue), and  $-f_{\text{rad-corr}}^R$  (green) at  $z = 300r_s$ . The radiation drag

force dominates over the radiation flux force and the relativistic correction except at  $R \leq 20r_S$ , where the inward ( $-R$  direction) radiation flux force is dominant. Hence, the expansion of the outflow is prevented by the radiation drag at  $R \gtrsim 80r_S$ . We conclude that the radiation drag force has important roles for determining both the velocity and the opening angle of the outflow.

#### 4. Conclusions and Discussion

We performed 2.5-dimensional special relativistic radiation magnetohydrodynamics simulations to study the super-critical accretion disks and the radiatively driven outflows. We found that the outflow is accelerated by the radiation flux force and is subjected to the radiation drag force, which prevents the outflow from speeding up. The outflow velocity is determined by force balance between above two forces and becomes 30–40% of the light speed near the rotation axis. Such a velocity does not change so much in the super-critical accretion regime of  $\dot{M}_{\text{BH}} \sim 10^2 - 10^3 L_{\text{Edd}}$ .

Such a faster outflow is surrounded by a slower outflow, of which the velocity is  $\sim 0.1$ . It is similar with so-called spine-sheath structure. It is found that the radiation drag force works to collimate the slower outflow in cooperation with the Lorentz force, though the faster outflow is mainly collimated by the Lorentz force. The most of kinetic energy is carried by the slower outflow, and the radiation energy is larger in the slower outflow than in the faster outflow. Although the mass accretion rate onto the black hole largely exceeds the critical rate ( $L_{\text{Edd}}$ ), the total photon and kinematic luminosities are comparable to  $L_E$ , since a huge amount of the radiation energy is trapped and swallowed by the black hole with accreting matter. The swallowed photon luminosity is roughly proportional to the mass accretion rate.

The resulting outflow velocity of  $\sim 0.3 - 0.4$  nicely agrees with the jets ( $\sim 0.26$ ) observed in SS 433 (Marshall et al. 2002). However, it is inconsistent with the highly relativistic jets in GRS 1915+195 (Mirabel & Rodríguez 1994; Fender et al. 1999), or some active galactic nuclei (Biretta et al. 1995; Giroletti et al. 2012). The outflow velocity might increase if the slower outflow is optically thick. This is because the outflow is self-shielded and the spine of the outflow can avoid suffering from the radiation drag. In addition, if the photon bubble instability occurs near the innermost regions of the accretion disks, the outward radiation flux increases, going up the outflow velocity due to the enhanced radiation flux force (Begelman 1978; Turner et al. 2005). On the other hand, the outflow velocity does not increase even if the pair-plasma appears in the outflow, since the radiation drag acts on the positron as well as the electron.

We included only opacities due to the electron scattering and free-free absorption. Recently, Kawashima et al. (2009) performed non-relativistic radiation hydrodynamic simulations including thermal Comptonization. They showed that although the Compton effect does not impact on the disk structure so much, the gas temperature of the outflow drastically decreases due to the Compton up-scattering. Decreasing of the gas temperature leads to softening of X-ray spectrum (Kawashima et al. 2012). We need to include the Comptonization in rel-

ativistic radiation MHD simulation Sadowski et al. (2014) to explain the spectral properties observed in microquasars.

Although we assume the axisymmetry in the present study, three-dimensional study is required in order to estimate the outflow velocity more precisely. If the density of the disk fluctuates in azimuthal direction, the photon trapping effect might degrade since the photon can escape from the less dense region. Then, the radiation fields change and the outflow velocity alters. The dynamo would change the evolution of the magnetic fields, leading to the change of the disk structure. The saturation velocity in such a case might be differ from that of the present study. The 3-dimensional simulation has been initiated in the Newtonian limit (Jiang et al. 2014a) and in general relativity (McKinney et al. 2014). Jiang et al. (2014a) performed 3-dimensional simulation of slim disks by solving full radiation transfer equation keeping terms of  $\mathcal{O}(v)$ . They found that the outflow velocity is about 0.3, which is consistent with our results. Comparing results in detail between these different models is also very important future work to understand the validity of the closure relation.

The light bending should decrease the photon luminosity, since more photons are swallowed by the black hole. Then, the kinetic luminosity of the outflow would go down. In contrast, the spin of the black hole is though to enhance the outflow (e.g., Blandford & Znajek 1977). Recently, GR simulations have been revealed that the strong outflow is generated from the super-critical accretion disks around Kerr black hole (Sądowski et al. 2014; McKinney et al. 2014).

Finally, we discuss the difference between our simulations and previous non-relativistic simulations. Takeuchi et al. (2010) performed non-relativistic radiation MHD simulation with the flux-limited diffusion approximation (FLD, Levermore & Pomraning (1981)), reporting that the outflow velocity is about 0.6–0.7, which is faster than our results ( $\sim 0.4$ ). Such a difference would be caused by the radiation drag effect, which is not taken into account in Takeuchi et al. (2010). Thus, we stress that it is important to include the radiation drag effects to study acceleration mechanisms of outflows from black hole accretion disks.

The different algorithms make differences especially in the outflow regions, since the approximate radiative transfer algorithms (e.g., FLD approximation, the Eddington approximation, and the M-1 method) are known to be problematic in the optically thin region and, in contrast, give accurate radiation fields in the optically thick diffusion limit. The FLD approximation cannot be properly applied to the relativistic fluid since it violates a causality (e.g., the radiation energy equation becomes parabolic). On the other hand, the Eddington approximation is utilizable in relativistic simulations. In the relativistic one-dimensional test problems, (Takahashi & Ohsuga 2013) showed that  $F'_{\text{rad}}/E'_{\text{rad}}$  becomes larger for the M-1 treatment than for the Eddington approximation. Thus, it is expected that the terminal velocity becomes slower if the Eddington approximation is adopted. However, the performing simulation with the Eddington approximation is time-consuming since  $6 \times 6$  matrix inversion at each grid point is needed to compute Eddington tensor. Hence, the detailed comparison between Eddington approximation and M-1 closure is beyond the scope of the present paper and is left as an important future work.



In addition, recently, a more accurate method, which solves radiative transfer equation, has been proposed by Jiang et al. (2014b). Comparing results between these different models is also very important future work to understand the validity of the closure relation.

We are grateful to an anonymous referee for improving our manuscript. We thank T. Kawashima for useful discussion. Numerical computations were carried out on Cray XC30 at the Center for Computational Astrophysics, CfCA, at the National Astronomical Observatory of Japan, and on T2K at the University of Tokyo. This work is supported in part by Ministry of Education, Culture, Sports, Science, and Technology (MEXT) for Young Scientist (B) 24740127 (K.O.). A part of this research has been funded by MEXT HPCI STRATEGIC PROGRAM and the Center for the Promotion of Integrated Sciences (CPIS) of Sokendai.

## References

- Abdo, A. A., Ackermann, M., Arimoto, M., Asano, K., Atwood, W. B., Axelsson, M., Baldini, L., Ballet, J., Band, D. L., Barbiellini, G., & et al. 2009, *Science*, 323, 1688
- Abramowicz, M. A., Czerny, B., Lasota, J. P., & Szuszkiewicz, E. 1988, *ApJ*, 332, 646
- Begelman, M. C. 1978, *MNRAS*, 184, 53
- Biretta, J. A., Zhou, F., & Owen, F. N. 1995, *ApJ*, 447, 582
- Blandford, R. D. & Znajek, R. L. 1977, *MNRAS*, 179, 433
- Bucciantini, N. & Del Zanna, L. 2013, *MNRAS*, 428, 71
- Bugli, M., Del Zanna, L., & Bucciantini, N. 2014, *MNRAS*, 440, L41
- Cowling, T. G. 1933, *MNRAS*, 94, 39
- Farris, B. D., Li, T. K., Liu, Y. T., & Shapiro, S. L. 2008, *Phys. Rev. D*, 78, 024023
- Fender, R. P., Garrington, S. T., McKay, D. J., Muxlow, T. W. B., Pooley, G. G., Spencer, R. E., Stirling, A. M., & Waltman, E. B. 1999, *MNRAS*, 304, 865
- Giroletti, M., Hada, K., Giovannini, G., Casadio, C., Beilicke, M., Cesarini, A., Cheung, C. C., Doi, A., Krawczynski, H., Kino, M., Lee, N. P., & Nagai, H. 2012, *A&A*, 538, L10
- Hawley, J. F. & Balbus, S. A. 1991, *ApJ*, 376, 223
- Ichimaru, S. 1977, *ApJ*, 214, 840
- Igumenshchev, I. V. 2008, *ApJ*, 677, 317
- Igumenshchev, I. V., Narayan, R., & Abramowicz, M. A. 2003, *ApJ*, 592, 1042
- Jiang, Y.-F., Stone, J. M., & Davis, S. W. 2014a, *ArXiv e-prints* — 2014b, *ApJS*, 213, 7
- Kato, S., Fukue, J., & Mineshige, S. 2008, *Black-Hole Accretion Disks — Towards a New Paradigm —*, ed. Kato, S., Fukue, J., & Mineshige, S.
- Kawashima, T., Ohsuga, K., Mineshige, S., Heinzeller, D., Takabe, H., & Matsumoto, R. 2009, *PASJ*, 61, 769
- Kawashima, T., Ohsuga, K., Mineshige, S., Yoshida, T., Heinzeller, D., & Matsumoto, R. 2012, *ApJ*, 752, 18
- Levermore, C. D. & Pomraning, G. C. 1981, *ApJ*, 248, 321
- Marshall, H. L., Canizares, C. R., & Schulz, N. S. 2002, *ApJ*, 564, 941
- McKinney, J. C., Tchekhovskoy, A., Sądowski, A., & Narayan, R. 2014, *MNRAS*, 441, 3177
- Meier, D. L. 2003, *New A Rev.*, 47, 667
- Mirabel, I. F. & Rodríguez, L. F. 1994, *Nature*, 371, 46
- Narayan, R. & Yi, I. 1994, *ApJ*, 428, L13
- Ohsuga, K. & Mineshige, S. 2007, *ApJ*, 670, 1283
- . 2011, *ApJ*, 736, 2
- Ohsuga, K., Mineshige, S., Mori, M., & Kato, Y. 2009, *PASJ*, 61, L7+
- Ohsuga, K., Mineshige, S., Mori, M., & Umemura, M. 2002, *ApJ*, 574, 315
- Ohsuga, K., Mineshige, S., & Watarai, K.-y. 2003, *ApJ*, 596, 429
- Ohsuga, K., Mori, M., Nakamoto, T., & Mineshige, S. 2005, *ApJ*, 628, 368
- Paczynski, B. & Wiita, P. J. 1980, *A&A*, 88, 23
- Roedig, C., Zanotti, O., & Alic, D. 2012, *MNRAS*, 426, 1613
- Rykoff, E. S., Aharonian, F., Akerlof, C. W., Ashley, M. C. B., Barthelmy, S. D., Flewelling, H. A., Gehrels, N., Göğüş, E., Güver, T., Kiziloğlu, Ü., Krimm, H. A., McKay, T. A., Özel, M., Phillips, A., Quimby, R. M., Rowell, G., Rujopakarn, W., Schaefer, B. E., Smith, D. A., Vestrand, W. T., Wheeler, J. C., Wren, J., Yuan, F., & Yost, S. A. 2009, *ApJ*, 702, 489
- Sądowski, A., Narayan, R., Tchekhovskoy, A., Abarca, D., Zhu, Y., & McKinney, J. C. 2014, *ArXiv e-prints*
- Sądowski, A., Narayan, R., McKinney, J. C., & Tchekhovskoy, A. 2014, *MNRAS*, 439, 503
- Sądowski, A., Narayan, R., Tchekhovskoy, A., & Zhu, Y. 2013, *MNRAS*, 429, 3533
- Shakura, N. I. & Sunyaev, R. A. 1973, *A&A*, 24, 337
- Sol, H., Pelletier, G., & Asseo, E. 1989, *MNRAS*, 237, 411
- Takahashi, H. R. & Ohsuga, K. 2013, *ApJ*, 772, 127
- Takahashi, H. R., Ohsuga, K., Sekiguchi, Y., Inoue, T., & Tomida, K. 2013, *ApJ*, 764, 122
- Takeuchi, S., Ohsuga, K., & Mineshige, S. 2010, *PASJ*, 62, L43+
- Turner, N. J., Blaes, O. M., Socrates, A., Begelman, M. C., & Davis, S. W. 2005, *ApJ*, 624, 267
- Zanotti, O., Roedig, C., Rezzolla, L., & Del Zanna, L. 2011, *MNRAS*, 417, 2899